Computations of Magnus Effects for a Yawed, Spinning Body of Revolution

Walter B. Sturek,* Harry A. Dwyer,† Lyle D. Kayser,* Charles J. Nietubicz,*
Robert P. Reklis,‡, and Klaus O. Opalka§
U.S. Army Ballistic Research Laboratory, Aberdeen Proving Ground, Md.

Many projectiles used by the Army are slender bodies of revolution which are launched at high spin rates. Magnus forces and moments are generated by the distorted boundary layer which results from a spinning body at angle of yaw. This paper reports the results of a combined theoretical-experimental research effort to develop a method for computing Magnus effects that would be useful in the design of artillery projectiles. The theoretical effort involves: 1) numerical calculation of the fully three-dimensional boundary layer with the added complication of interaction between surface spin and cross flow velocity; and 2) three-dimensional inviscid flow calculations over a body plus boundary-layer displacement surface with no plane of symmetry. Experimental measurements of turbulent boundary-layer profile characteristics, wall static pressure, and aerodynamic forces have been obtained to evaluate and provide guidance to the theoretical effort. Comparisons between the theory and the experimental data indicate very close agreement and substantiate the validity of the theoretical approach.

Nomenclature

c_f = skin friction coefficient
c_p = specific heat at constant pressure
C_N = normal force coefficient
C_Y = Magnus (side) force coefficient
D = diameter of base of model
h = static enthalpy
k_t = turbulent conductivity
ℓ = mixing length
p = pressure
P = spin rate, rad/s
Pr_t = turbulent Prandtl number, $c_p\epsilon/k_t$
r = local radius of model
Re_ℓ = Reynolds number based on model length
u,v,w = velocities in boundary-layer coordinates
V = velocity along model trajectory
x = surface coordinate in longitudinal direction
y,Y = coordinate perpendicular to local surface
z = cylindrical coordinate along model axis
α = angle of attack
ϵ = turbulent eddy viscosity
δ = boundary-layer thickness
δ^* = boundary-layer displacement thickness
Δp = centrifugal pressure gradient contribution to side force
η = transformed y coordinate
μ = molecular viscosity
ξ = transformed x coordinate
ρ = density
τ_x = longitudinal velocity wall shear contribution to side force
τ_ϕ = circumferential velocity wall shear contribution to side force
ϕ = coordinate in circumferential (azimuthal) direction

Subscripts

e = edge of boundary layer
w = model wall conditions
x = quantity in x direction
∞ = freestream reference condition
ϕ = quantity in azimuthal direction

Superscripts

$(\,)'$ = fluctuating quantity
$\overline{(\,)}$ = time-averaged quantity

Received Oct. 13, 1977; revision received Feb. 16, 1977.

Index categories: Boundary Layers and Convective Heat Transfer—Turbulent; Jets, Wakes, and Viscid-Inviscid Flow Interactions; Supersonic and Hypersonic Flow.

*Aerospace Engineer, Launch and Flight Division. Member AIAA.
†Consultant, Launch and Flight Division; also Professor, University of California at Davis. Member AIAA.
‡Physicist, Launch and Flight Division.
§Aerospace Engineer, Terminal Ballistics Division.

I. Introduction

MANY projectiles used by the Army are slender, spin-stabilized bodies of revolution. Magnus forces and moments are generated by the distorted boundary layer which results from a spinning body at angle of yaw. Recent Army interest in achieving increased range and greater payload capacity in artillery projectiles has led to designs with long, slender ogives, increased projectile length, and boattailed afterbodies. These designs have resulted in decreased drag with a resulting increase in range; however, the gyroscopic stability of these shapes is less than that of more conventional designs. This means that these new shapes are more susceptible to a Magnus-induced instability. The Magnus force is small (Fig. 1), typically 1/10 to 1/100 of the normal force; however, its effect is important because the Magnus moment can be of sufficient magnitude to cause the projectile to become dynamically unstable. Thus, it is desirable to minimize the Magnus moment in order for the projectile to fly at a small average angle of attack and achieve the greatest range capability.

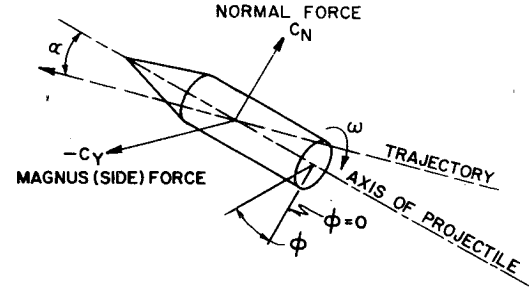

Fig. 1 Magnus and normal forces on a spinning projectile.

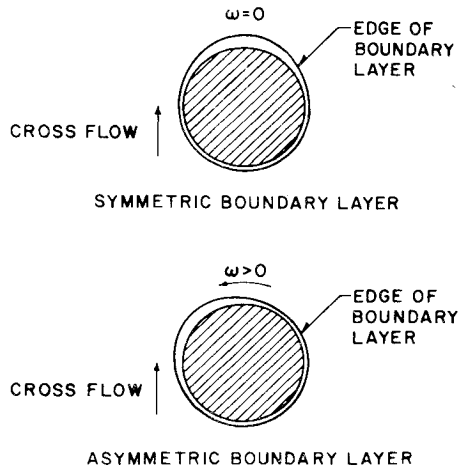

Fig. 2 Schematic illustration of spin-induced boundary-layer distortion.

The Magnus effect has been modeled theoretically as resulting from spin-induced distortion of the boundary layer. This effect is illustrated schematically in Fig. 2 where a cross-sectional view of a body of revolution is shown. The body is at angle of attack as indicated by the cross-flow velocity. In the view where there is no surface spin, the profile of the edge of the boundary layer is symmetric with respect to the plane of the angle of attack. In the view where the surface is spinning, the profile of the boundary layer is asymmetric with respect to the plane of the angle of attack. Thus, the inviscid pressure distribution (which responds to the aerodynamic shape composed of the model plus the boundary-layer displacement surface) is asymmetric and yields a net side force.

A method for predicting Magnus effects has been sought for many years.[1-8] The techniques developed have used some empiricism and/or slender body theory, except for the technique of Dwyer and Sanders,[7,8] which is limited to the laminar boundary layer on a sharp-nosed cone. In this report, the results of recent efforts to extend the technique of Dwyer and Sanders to turbulent boundary layer and more general body configurations such as an ogive cylinder are described. Experimental data consisting of detailed turbulent boundary-layer profile characteristics and aerodynamic force measurements have been obtained to help guide the development of the theoretical effort. Comparisons of the computations to these unique data represent the first such comparisons for the compressible turbulent boundary layer on a yawed, slender body of revolution. The computations of Magnus effects are the first computations for a realistic projectile configuration in a conceptually "exact" manner.

II. Theoretical Approach

A. Background

Since the Magnus effect is a viscous phenomenon, computation of the boundary-layer development is the foundation for computations of the Magnus force. The boundary layer we are considering is fully three-dimensional with the added complication of the interaction of surface spin with the cross-flow velocity. The inviscid flow also requires special attention since, in order to compute the Magnus force, the inviscid flow computation technique must be able to compute the 3-D flow over a body plus the boundary-layer displacement surface with no plane of symmetry.

B. Boundary-Layer Computations

The basic equations defining the three-dimensional compressible, turbulent boundary-layer flow over an axisymmetric body of revolution described by the relation $r=r(x)$ are listed below. The coordinate system is shown in Fig. 3.

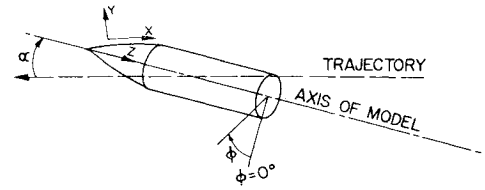

Fig. 3 Coordinate system.

Continuity

$$\frac{\partial}{\partial x}(r\bar{\rho}\bar{u}) + \frac{\partial}{\partial y}(r\bar{\rho}\hat{v}) + \frac{\partial}{\partial \phi}(\bar{\rho}\bar{w}) = 0 \tag{1}$$

x momentum

$$\bar{\rho}\left[\bar{u}\frac{\partial \bar{u}}{\partial x} + \hat{v}\frac{\partial \bar{u}}{\partial y} + \frac{\bar{w}}{r}\frac{\partial \bar{u}}{\partial \phi} - \frac{\bar{w}^2}{r}\frac{\partial r}{\partial x}\right] = -\frac{\partial \bar{p}_e}{\partial x} + \frac{\partial}{\partial y}\left[\mu\frac{\partial \bar{u}}{\partial y} - \bar{\rho}\overline{u'v'}\right] \tag{2}$$

ϕ momentum

$$\bar{\rho}\left[\bar{u}\frac{\partial \bar{w}}{\partial x} + \hat{v}\frac{\partial \bar{w}}{\partial y} + \frac{\bar{w}}{r}\frac{\partial \bar{w}}{\partial \phi} + \frac{\bar{u}\bar{w}}{r}\frac{\partial r}{\partial x}\right] = -\frac{1}{r}\frac{\partial \bar{p}_e}{\partial \phi} + \frac{\partial}{\partial y}\left[\mu\frac{\partial \bar{w}}{\partial y} - \bar{\rho}\overline{v'w'}\right] \tag{3}$$

Energy

$$\bar{\rho}\left[\bar{u}\frac{\partial \bar{h}}{\partial x} + \hat{v}\frac{\partial \bar{h}}{\partial y} + \frac{\bar{w}}{r}\frac{\partial \bar{h}}{\partial \phi}\right] = \bar{u}\frac{\partial \bar{p}_e}{\partial x} + \frac{\bar{w}}{r}\frac{\partial \bar{p}_e}{\partial \phi} + \mu\left[\left(\frac{\partial \bar{u}}{\partial y}\right)^2 + \left(\frac{\partial \bar{w}}{\partial y}\right)^2\right] - \bar{\rho}\overline{u'v'}\frac{\partial \bar{u}}{\partial y} - \bar{\rho}\overline{v'w'}\frac{\partial \bar{w}}{\partial y} + \frac{\partial}{\partial y}\left[\frac{\mu}{\mathrm{Pr}}\frac{\partial \bar{h}}{\partial y} - \bar{\rho}\overline{v'h'}\right] \tag{4}$$

where $\hat{v} = \bar{v} + \overline{\rho' v'}/\bar{\rho}$ and the bar indicates a time-averaged quantity.

In order to obtain closure of this system of equations, the following models of the turbulence terms have been introduced:

Turbulent shear stress

$$-\bar{\rho}\overline{u'v'} = -\bar{\rho}\overline{v'w'} = \bar{\rho}\ell^2\left[\left(\frac{\partial \bar{u}}{\partial y}\right)^2 + \left(\frac{\partial \bar{w}}{\partial y}\right)^2\right] = \epsilon\left[\left(\frac{\partial \bar{u}}{\partial y}\right)^2 + \left(\frac{\partial \bar{w}}{\partial y}\right)^2\right]^{1/2}$$

where ϵ is introduced as the turbulent viscosity and the mixing length, $\ell = 0.09\,\delta\tanh[(0.4/0.09)(y/\delta)]$. Van Driest damping is used to account for the effect of the laminar sublayer.

Turbulent heat transfer

$$-\bar{\rho}\overline{v'h'} = \frac{k_t}{c_p}\frac{\partial \bar{h}}{\partial y}$$

The turbulent Prandtl number is introduced as

$$Pr_t = c_p\epsilon/k_t = 0.90$$

The numerical technique used to solve these equations is an implicit technique developed by Dwyer[7,9] that takes into consideration the changes in direction of the cross-flow velocity that occurs on the side of the model where the inviscid cross flow opposes surface spin. This technique correctly models the cross-flow convection process occurring within the boundary layer. In order to improve the speed and accuracy of the numerical solution, several coordinate transformations are employed:

1) Mangler transformation of axisymmetric growth

$$\xi = \int_0^x r^2 dx$$

2) Blasius type transformation of normal growth

$$\eta = \left(\frac{p_\infty}{p_e}\right)^{1/2} \left(\frac{\rho_\infty u_\infty}{2\mu_\infty \xi}\right)^{1/2} \int_0^y \frac{\rho}{\rho_\infty} r dy$$

3) Coordinate stretching to allow closer grid spacing near the wall[10]

$$n_j = 100(1.5\exp[(j-1)(1/60)(1/0.05)] - 1)/(1.5\exp(1/0.05) - 1)$$

where $j = 1, 2, 3, \ldots 61$.

In computing the boundary-layer development, the effect of turbulence is turned on gradually over three longitudinal steps. The computation grid in the azimuthal plane is in 10-deg increments. Three iterations are performed at each station for turbulent computations. For comparison with experiment, the location of boundary-layer transition is fixed at the boundary-layer trip on the experimental model.

C. Three-Dimensional Displacement Surface

The three-dimensional displacement surface is not merely the vector sum of the longitudinal and circumferential components of the boundary-layer displacement thicknesses. Instead, the differential equation derived by Moore[11]:

$$\frac{\partial}{\partial x}[\rho_e u_e r(\delta^*_{3\text{-D}} - \delta^*_x)] + \frac{\partial}{\partial \phi}[\rho_e w_e(\delta^*_{3\text{-D}} - \delta^*_\phi)] = 0 \qquad (5)$$

must be solved for $\delta^*_{3\text{-D}}$, the three-dimensional boundary-layer displacement thickness where

$$\delta^*_x = \int_0^\delta \left(1 - \frac{\rho u}{\rho_e u_e}\right) dy$$

and

$$\delta^*_\phi = \int_0^\delta \left(1 - \frac{\rho w}{\rho_e w_e}\right) dy$$

Dwyer[12] has shown that Eq. (5) is of the general form

$$P\frac{\partial \delta^*_{3\text{-D}}}{\partial x} + Q\frac{\partial \delta^*_{3\text{-D}}}{\partial \phi} = R_1 \delta^*_{3\text{-D}} + R_2 \qquad (6)$$

The singularity in $\delta^*_{3\text{-D}}$ and δ^*_x at $x=0$ can be avoided by starting the computations at a small, finite value of x and computing approximate starting conditions. Equation (6) can then be solved as an ordinary differential equation, providing the differencing in the circumferential direction is carried out from $\phi = 0$ to 180 deg and from $\phi = 0$ to -180 deg in order to obey the zone of influence defined by

$$dx/d\phi = r(u_e/w_e)$$

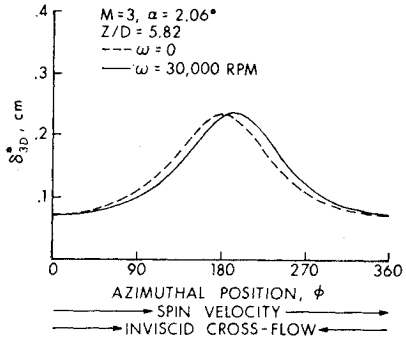

Fig. 4 Computations of $\delta^*_{3\text{-D}}$ for the SOC model, $\omega = 30{,}000$ rpm.

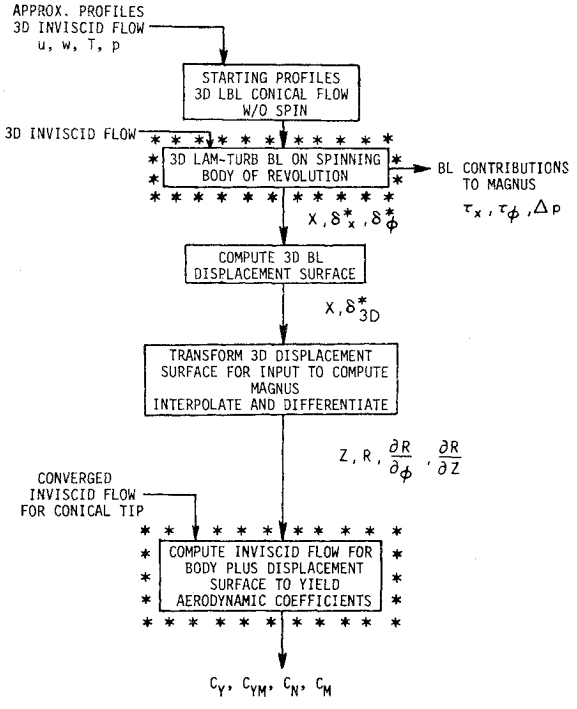

Fig. 5 Sequence of numerical computations.

An example of computed values of $\delta^*_{3\text{-D}}$ for the SOC model is shown in Fig. 4. The effect of spin is to decrease the thickness of the boundary layer where surface spin and inviscid cross flow are in the same direction and to increase the thickness of the boundary layer where surface spin and inviscid flow oppose.

D. Inviscid Computations

The development of a numerical technique for computing the 3-D inviscid flowfield over a yawed, pointed body in supersonic flow was a very important step in the development of a capability for computing Magnus effects.[8] The program uses MacCormack's[13] "shock capturing" numerical technique. This is a second-order accurate scheme that uses a predictor-corrector technique to solve the equations of motion in an implicit marching scheme. The unique feature of the program, developed by Sanders for the Magnus problem, is that the flowfield is computed about an axisymmetric model plus displacement surface which, due to the distortion of the boundary layer by surface spin, has no plane of symmetry.

E. Sequence of Computations

The sequence of computations which must be run in order to compute Magnus effects is indicated in Fig. 5. Each block indicates a separate computer program along with its required input information and the output. The two main programs are outlined in asterisks.

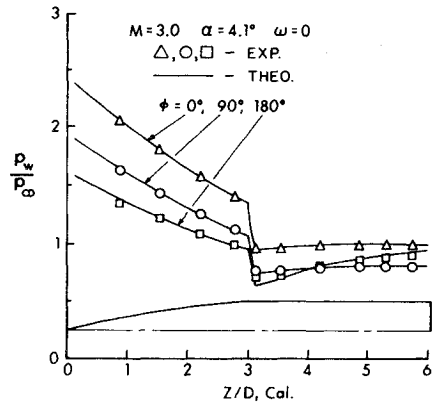

Fig. 6 Surface pressure distribution on the SOC model.

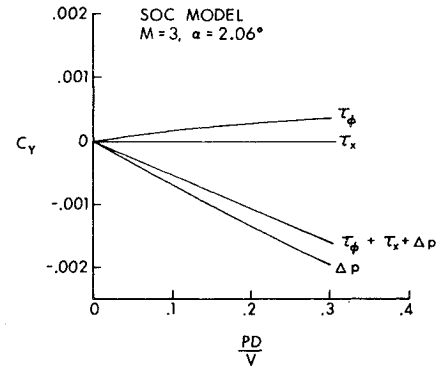

Fig. 7 Turbulent boundary-layer contributions to Magnus force, $Z/D=5.82$.

In order to start the computations, an initial plane of profile data at the tip of the model and inviscid flow boundary conditions are required. The initial profile data are computed for the limiting condition of the conical tip of the model. The inviscid flow boundary conditions are computed using the program developed by Sanders.[8] An example showing the computed wall pressure distribution compared to experimental data for several azimuthal stations is shown in Fig. 6. Also shown is the outline of the model shape, a 6-caliber-long secant-ogive cylinder. As seen in the figure, excellent agreement is obtained between theory and experiment for the moderate angle of attack considered here. It is seen that the boundary layer experiences a significant history of favorable and adverse pressure gradients in both the longitudinal and circumferential directions.

In order to start the boundary-layer computation for the spinning model, initial profile data are generated for the limiting case of the laminar boundary layer at the tip of a nonspinning cone. These data, along with the outer boundary condition of the inviscid flow, enable the marching technique to begin for specific conditions of Mach number, angle of attack, wall temperature, spin rate, and freestream properties. The output of the boundary-layer program consists of wall shear and centrifugal pressure gradient contributions to the Magnus effect and the longitudinal and circumferential components of the boundary-layer displacement surface as functions of longitudinal and circumferential position over the entire surface of the model.

The output of the boundary-layer program is input to the program which solves for the three-dimensional boundary-layer displacement thickness, $\delta^*_{3\text{-}D}$. Input data for this program are in the surface coordinate system used for the boundary-layer computations. The output of this program is transformed into a cylindrical coordinate system, in order to facilitate computation of the inviscid flow. The output consists of the surface coordinates of the model plus $\delta^*_{3\text{-}D}$, as well as the local derivatives of the surface coordinate plus $\delta^*_{3\text{-}D}$ in the axial and circumferential directions.

The final step is the computation of the inviscid flow over the newly defined body, which is of completely arbitrary configuration with no plane of symmetry. The starting conditions consist of the inviscid flowfield for the asymptotic cone tip of the original model. Pitch and yaw plane force and moment aerodynamic coefficients are the final outputs obtained.

F. Boundary-Layer Components of Magnus

Due to spin-induced asymmetry in the computed velocity profiles, three contributions to the Magnus effect are generated at the surface of the spinning model which must be added to the boundary-layer displacement effect sensed by the outer inviscid flow. These components are: 1) longitudinal velocity wall shear, $\tau_x=\mu(\partial u/\partial y)_{y=0}$; 2) circumferential velocity wall shear, $\tau_\phi=\mu(\partial w/\partial y)_{y=0}$; and 3) centrifugal pressure gradient, $\Delta p=\int_0^y(\rho w^2/r)dy$. For a nonspinning model, the net contribution of each of these components would be zero. However, due to the asymmetry induced by surface spin, a small contribution to a side force is obtained. The relative magnitudes of these components of the Magnus force are shown in Fig. 7.

III. Experimental Measurements

A. General

The purpose of the experimental studies is to provide data that will be useful in evaluating and providing guidance for the theoretical effort. The experimental studies consisted of: 1) boundary-layer profile measurements; 2) optical studies; 3) Preston tube skin friction measurements; 4) strain-gage balance force measurements; and 5) wall static pressure measurements. Only the boundary-layer profile measurements and aerodynamic force measurements will be described here.

Experimental results were obtained in the Ballistic Research Laboratory supersonic wind tunnel no. 1, which is a continuous flow, flexible nozzle tunnel capable of Mach numbers 1.5-5.0; the test section size is 38 cm high by 33 cm wide. Data were obtained at Mach 3.0, a Reynolds number (Re_l) of 7.6×10^6 and at both spinning and nonspinning conditions.

The model tested was the 6-caliber, secant-ogive cylinder with geometry as shown in the pressure distribution plot of Fig. 6. The model was equipped with a boundary-layer trip located 0.7 caliber from the nose to insure a consistent turbulent flow for all tests.

B. Boundary-Layer Measurements

Measurements of the total head pressure through the boundary layer were made with a flattened impact pressure probe 0.15 cm wide by 0.015 cm high. Data were obtained on the cylindrical section at 3.33, 4.44, and 5.56 calibers from the nose and azimuthally around the model in 30-deg increments and at yaw angles from 0 to 6.3 deg. At each position, surveys were made at both 0 and 20,000 rpm; the spin rate of 20,000 rpm corresponds to a PD/V of 0.19. The impact pressure probe was brought from outside the boundary layer down to and contacting the model surface for the 0 rpm case; for the 20,000 rpm spin rate the probe was brought down to within approximately 0.01 cm from the surface. The probe axis was aligned longitudinally with the model axis. Some uncertainty is inherent in the profile data because the probe is not aligned with the local flow direction within the boundary layer. This uncertainty would be greatest near the surface of the model and at longitudinal stations near the forward portion of the model. However, the large gradients present in a turbulent boundary layer would confine the greatest effect of flow angularity to a very small region near the surface, which cannot be accurately probed using a total head probe. Also, these measurements were obtained at small angles of attack.

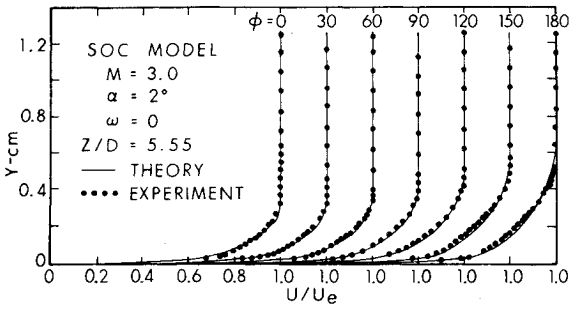

Fig. 8 Velocity profiles, theory compared with experiment.

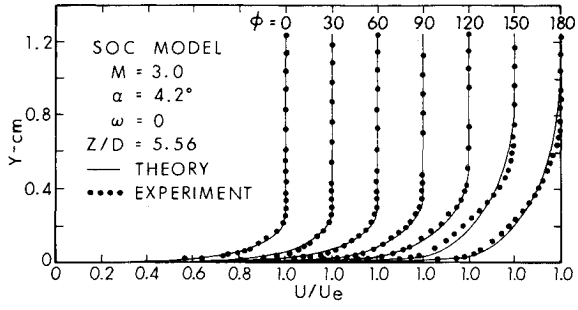

Fig. 9 Velocity profiles, theory compared with experiment.

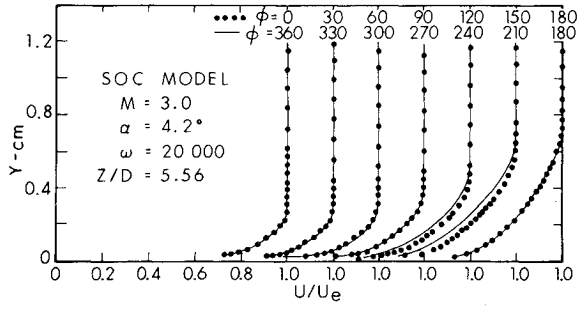

Fig. 10 Experimental velocity profiles, effects of spin.

The local flow Mach number within the boundary layer was determined using the Rayleigh pitot formula, assuming constant static pressure through the boundary layer equal to the measured wall static pressure.

C. Force Measurements

Measurements of Magnus and normal force were obtained using the strain-gage balance technique. The model is free to rotate on internally mounted bearings and equipped with a single row of turbine blades so that spin-up can be achieved. Turbine air is supplied to the model through the sting and the model is brought up to speeds as high as 40,000 rpm. The turbine air is then cut off and data are acquired as the model spin rate decays.

IV. Comparison of Theory and Experiment

A comparison of theoretical and experimental velocity profiles is shown in Fig. 8 for 2-deg angle of attack and zero spin rate. The agreement is considered to be good and is actually comparable to that obtained for supersonic two-dimensional flow measurements. On the leeward side, near $\phi = 180$ deg, the theoretical velocities are greater than the experimental measurements near the surface, and the theoretical velocities are smaller than the experimental velocities near the edge of the boundary layer. On the windward side, near $\phi = 0$ deg, the situation is reversed. These differences in profile shape will give compensating effects

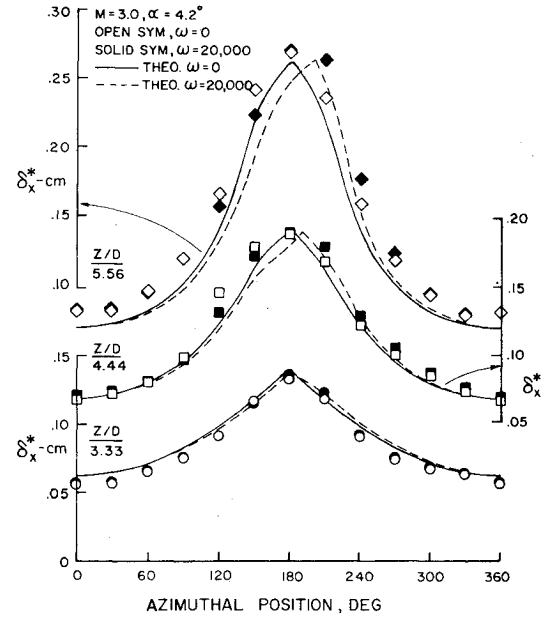

Fig. 11 Boundary-layer displacement thickness, δ_x^*, theory compared with experiment, SOC model.

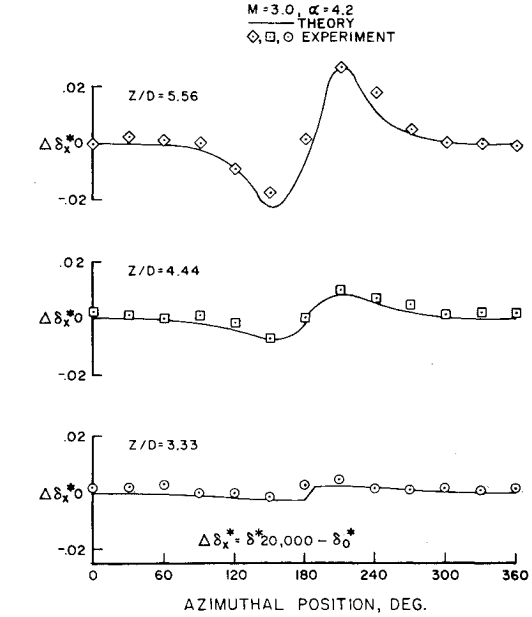

Fig. 12 Increment of displacement thickness, $\Delta\delta_x^*$, due to spin, SOC model, theory compared with experiment.

when computing integral parameters. Figure 9 compares theoretical and experimental velocity profiles at 4.2-deg angle of attack. The differences between theoretical and experimental profile shape are similar to those at $\alpha = 2$ deg, except that they are more pronounced; also, the variation in boundary-layer thickness from the windward to the leeward side is greater for the 4.2-deg case.

The effect of spin on velocity profiles is shown in Fig. 10, where profiles on the side where cross flow and spin are in the same direction ($\phi = 0$-180) are compared with profiles on the opposite side of the model ($\phi = 180$-360) where the cross flow is in the opposite direction of spin. On the windward side of the model ($\phi = 0$-90), there is almost no measurable effect of spin. On the leeward side ($\phi = 120$ vs 240 and 150 vs 210), the profile shapes differ substantially. The effect of cross flow in opposition to model surface rotation (e.g., $\phi = 210$) is to decrease the fullness of the profile which, of course, will result in a larger displacement thickness. It is of interest to note that

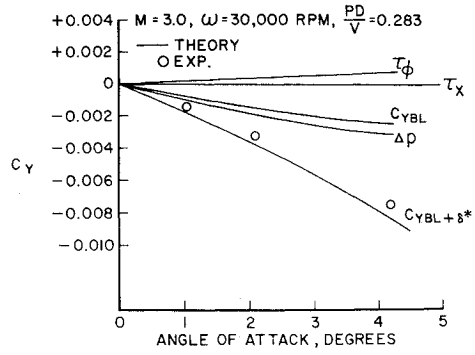

Fig. 13 Magnus force vs angle of attack, theory compared with experiment, SOC model, turbulent boundary layer.

the primary effect of spin is to change the profile shape rather than to change the total thickness.

Values for the longitudinal component of displacement thickness are compared in Fig. 11. The agreement between theory and experiment is generally good; however, it is seen at the forward station ($Z/D=3.33$) that the theoretical thicknesses are slightly greater than experiment ($\phi \approx 0$), and at the aft station theoretical thicknesses are slightly smaller than experiment. This situation indicates that the boundary layer actually grows at a faster rate than predicted by theory. The effect of spin on displacement thickness δ_x^* can be seen in Fig. 12, where the increment of δ_x^* due to spin is plotted on an expanded scale for $\alpha=4.2$ deg. The effect on displacement thickness is seen to be significant only in the vicinity of the leeward side ($\phi=180$ deg). The agreement between theory and experiment is encouraging evidence that the numerical technique accurately models the effect of surface spin.

One criterion which can be used to gage the success of the theory is the accuracy with which Magnus forces and moments can be predicted. Figure 13 is a comparison of theoretical and experimental Magnus forces; in addition, the magnitude of the four components of the Magnus force are shown. The contributions of τ_ϕ and Δp oppose and are of comparable magnitude, while the contribution of τ_x is minimal. The arithmetic sum of the three boundary-layer components is indicated by $C_{YBL}=\tau_x+\tau_\phi+\Delta p$. The total computed Magus force shown here is the arithmetic sum of the contributions due to $\tau_x, \tau_\phi, \Delta p$, and $\delta_{3\text{-}D}^*$. It is worthwhile to emphasize that this marks the first time that computations of the Magnus effect have been carried out in a conceptually "exact" manner for the turbulent boundary layer on a realistic projectile configuration. The agreement between the calculated Magnus force and experimental strain-gage balance force measurements is extremely good. The theoretical computations accurately reproduce the nonlinear trend of Magnus with angle of attack. This nonlinear behavior is primarily due to the increasing dominance of the contribution of $\delta_{3\text{-}D}^*$ as the angle of attack increases.

V. Concluding Remarks

A combined theoretical-experimental study of the Magnus effect on yawed, spinning projectiles has been discussed. The overall objective of this effort is to develop a method for computing Magnus effects that could be used in the design of artillery projectiles. Numerical techniques have been developed for computing: 1) the three-dimensional turbulent boundary-layer development over a yawed, spinning body of revolution; 2) the three-dimensional boundary-layer displacement surface for an arbitrary body of revolution; and 3) the three-dimensional inviscid flowfield over a yawed, pointed body of completely general configuration with no plane of symmetry. The computations have been compared to experimental measurements of Magnus force and turbulent boundary-layer profile characteristics. The general impression obtained in comparing the computations to experimental data is that the numerical techniques are working quite well and yielding very impressive agreement with experimental data. The results for Magnus force are considered extremely encouraging. The comparisons with detailed profile characteristics do reveal minor differences. It is believed that additional accuracy can be achieved by improved turbulence modeling. Other refinements in the boundary-layer computation, such as correction for transverse curvature and inclusion of boundary region effects, should be incorporated.

The ability to predict the point of transition may be a factor in the accuracy of the theoretical model. The location of transition was fixed by the use of boundary-layer trips for all the experiments described; therefore, the theoretical results do not reflect any error which might be caused in predicting the location of the transition line around the model.

References

[1] Martin, J. C., "On Magnus Effects Caused by Boundary Layer Displacement Thickness on Bodies of Revolution at Small Angles of Attack," BRL Rept. No. 870 (revised), U.S. Army Ballistic Research Lab., Aberdeen Proving Ground, Md., June 1955, AD 86858.

[2] Kelly, H. R. and Thacker, G. R., "The Effect of High Spin on the Magnus Force on a Cylinder at Small Angles of Attack," NAVORD Rept. No. 5036, U.S. Naval Ordnance Test Station, China Lake, Calif., Feb. 1956.

[3] Jacobson, I. D., "Influence of Boundary Layer Transition on the Magnus Effect on a Spinning Body of Revolution," Ph.D. dissertation, University of Virginia, June 1970.

[4] Vaughn, H. R. and Reis, G. E., "A Magnus Theory," *AIAA Journal*, Vol. 11, Oct. 1973, pp. 1396-1403.

[5] Graff, G. Y. and Moore, F. S., "The Effect of Boattail Shape on Magnus," NSWC/DL TR-3581, Dec. 1976.

[6] Lin, T. C. and Rubin, S. G., "Viscous Flow Over Spinning Cones at Angles of Attack," *AIAA Journal*, Vol. 12, July 1974, pp. 975-985.

[7] Dwyer, H. A. and Sanders, B. R., "Magnus Forces on Spinning Supersonic Cones. Part I; The Boundary Layer," *AIAA Journal*, Vol. 14, April 1976, p. 498; also, BRL Contract Rept. No. 248, July 1975, AD A013518.

[8] Sanders, B. R. and Dwyer, H. A., "Magnus Forces on Spinning Supersonic Cones. Part II: The Inviscid Flow," *AIAA Journal*, Vol. 14, May 1976, pp. 576-582.

[9] Dwyer, H. A., "Three Dimensional Flow Studies Over a Spinning Cone at Angle of Attack," BRL Contract Rept. No. 137, U.S. Army Ballistic Research Lab., Aberdeen Proving Ground, Md., Feb. 1974, AD 774795.

[10] Blottner, F. G., "Variable Grid Scheme Applied to Turbulent Boundary Layers," *Journal of Computer Methods in Applied Mechanics and Engineering*, Vol. 4, No. 2, 1974, pp. 179-194.

[11] Moore, F. N., "Displacement Effect of a Three-Dimensional Boundary Layer," NACA TN 2722, June 1952.

[12] Dwyer, H. A., "Methods for Computing Magnus Effects on Artillery Projectiles," BRL Contract Rept. No. 329, U.S. Army Ballistic Research Lab., Aberdeen Proving Ground, Md., Jan. 1977, AD A035330.

[13] MacCormack, R. W., "Numerical Solution of the Interaction of a Shock Wave With a Laminar Boundary Layer," *Lecture Notes in Physics*, Vol. 8, Maurice Holt, ed., Springer-Verlag, New York, 1971, pp. 151-163.